

Magnetotransport in ballistic graphene antidot lattices

Stephen R. Power¹⁻⁴, Morten Rishøj Thomsen², Antti-Pekka Jauho¹ and Thomas Garm Pedersen²

¹ Center for Nanostructured Graphene (CNG), DTU Nanotech, Department of Micro- and Nanotechnology, Technical University of Denmark, DK-2800 Kongens Lyngby, Denmark

² Center for Nanostructured Graphene (CNG), Department of Physics and Nanotechnology, Aalborg University, Skjernvej 4A, DK-9220 Aalborg East, Denmark

³ Catalan Institute of Nanoscience and Nanotechnology (ICN2), CSIC and The Barcelona Institute of Science and Technology, Campus UAB, Bellaterra, 08193 Barcelona (Cerdanyola del Vallès), Spain

⁴ Universitat Autònoma de Barcelona, 08193 Bellaterra (Cerdanyola del Vallès), Spain

E-mail: stephen.power@icn2.cat

E-mail: tgp@nano.aau.dk

March 2017

Abstract. Commensurability features in the magnetotransport properties of antidot lattices, emerging from correspondence between nanostructure feature size and electron cyclotron orbit, represent an archetypal mesoscopic physics phenomenon. Recent progress in experimental nanopatterning processes have led to the observation of distinct magnetoresistance commensurability peaks for graphene antidot lattices. In this work we develop a fully-atomistic, device-based simulation of the magnetoresistance measurements in such experiments, and complement this with detailed analysis of the current flow at commensurability conditions. A striking agreement with the experimental magnetoresistance spectra is produced. We further demonstrate that the simplest semi-classical view of *skipping* or *pinned* orbits cannot explain fully the flow of current in antidot systems. A generalised mechanism in terms of scattering between states bound to individual antidots, or groups of antidots, in a magnetic field is proposed. Commensurability features in magnetoresistance spectra are shown to be consistent with the enhanced scattering between such states. Finally, we examine the emergence and suppression of the commensurability peaks at different antidot sizes, and by tuning between classical and quantum regimes.

1. Introduction

High-quality graphene samples with very large carrier mobilities provide an excellent platform to explore a range of physical phenomena emerging from the unique linear band structure near the Dirac point, such as Klein tunneling [1, 2], the fractional quantum

Hall effect [3] and electron lensing [4, 5]. The ability to continuously tune the electron density in graphene using a back gate also allows for a range of mesoscopic phenomena, previously examined in semiconductor 2D electron gas systems, to be investigated more thoroughly and without the need for doping [6]. For example, the study of quantised conductance in confined one-dimensional channels relies on controlling the ratio of the system width and the Fermi wavelength. Typically, this involves changing the system width using gate-defined potentials at the channel edges, but can be achieved in graphene using a fixed-width nanoribbon and varying the Fermi wavelength via the electron density [7]. Ballistic graphene systems with variable electron densities are also ideal for probing mesoscopic classical physics effects – the realization of transverse magnetic focusing is a key example of this and allows electrons to be guided between two leads by varying their cyclotron radius in a magnetic field [8].

Antidot lattices provide perhaps the quintessential system for investigating two-dimensional mesoscopic phenomena [9–19]. They are realised in electron gases by a periodic array of strong repulsive potentials from which electrons travelling through the system are scattered. When Hall bar measurements are performed in the presence of a varying perpendicular magnetic field, a range of features are noted. When the cyclotron radius is large enough for electrons to scatter between antidots, successive scatterings can connect both sides of the device, reintroducing backscattering and removing the quantised edge transport of the quantum Hall regime (QHR). For most cyclotron radii in this regime, this leads to chaotic trajectories in the device bulk. However, when the cyclotron radius is commensurate with important system length scales, prominent new peaks and (non-quantised) plateaux emerge in the longitudinal and Hall resistances, R_{xx} and R_{xy} , respectively. These are typically associated with electron orbits which are i) *pinned* around individual or groups of antidots (shown by green circles in Fig. 1a) or ii) *skipping* between nearby antidots (also called *runaway* orbits and shown by the orange trajectory in Fig. 1a). Fine Aharonov-Bohm (AB) oscillations on top of these commensurability features are associated with quantisation of the electron orbits [20]. For high enough magnetic fields, the cyclotron radius is too small to cause scattering between antidots, and the QHR is mostly restored apart from exponentially suppressed quantum tunneling between states localised near individual antidots [21, 22].

Due to Klein tunneling [1], gate potentials are often inefficient at repelling electrons in graphene, and graphene antidot lattices (GALs) consist of periodic perforations of graphene sheets. The fabrication of such systems thus involves invasive techniques such as electron beam or block copolymer lithography [23–32]. The electronic properties of GALs and, in particular, the dependence of band gaps on geometry has been the subject of intensive research [33, 34]. Moreover, the influence of magnetic fields on perfectly periodic GALs and isolated antidots has been studied at the level of full atomistic approaches [35], the Dirac approximation [36], or the simple gapped graphene model [37]. Experimentally, a major issue is the deterioration of the graphene sheet quality and the difficulty in maintaining a uniform size and separation of antidots throughout the lattice. Indeed, the band gap behaviour predicted for certain lattice geometries [33, 34, 38–45] is

particularly sensitive to small levels of geometric disorder which may not be possible to eliminate in experiment [46–51]. Although such uniformity is not an essential ingredient for commensurability oscillations, invasive etching processes usually reduce the mean free path significantly so that electrons are principally scattered by defects and not antidots, thus suppressing commensurability effects. By encapsulating their graphene sheet in hexagonal boron nitride (hBN) during the nanopatterning step, Sandner *et al.* [52] demonstrated that the sample quality could be protected during the nanopatterning step and consequently they observed pronounced commensurability peaks which they associated with orbits around 1, 2, or 4 antidots in a square lattice. A contemporaneous study by Yagi *et al.* [53], using a different etching technique, found commensurability features in triangular lattices with smaller mean free paths, suggesting that scattering between nearest neighbour antidots plays a key role.

To clarify the mechanisms behind these commensurability peaks and determine the electron trajectories in such systems, we perform large-scale quantum mechanical transport simulations of graphene antidot lattice devices. A fully atomistic approach is employed, with direct measurement of longitudinal and Hall resistances taken from multi-terminal Hall bar geometries, as detailed in Section 2. The results of our simulations are shown in Section 3. As shown in Fig. 2 below, we find an exceptional agreement with the magnetotransport experimental results of Ref. [52], both in the relative positions and magnitudes of commensurability peaks. By mapping the current flow at commensurability peaks, we can identify the electron trajectories associated with each. We show that the classical picture of skipping or pinned orbits is too simple to fully describe the resulting electron flow patterns. An alternative analysis, in terms of scattering between states bound to individual antidots by the magnetic field, shows that a generalised skipping orbit picture can explain the first two commensurability peaks. Higher order peaks can be understood in terms of quasi-pinned orbits around groups of antidots. Both mechanisms act to divert electrons away from the sample edges and into the bulk, thus destroying the ballistic edge transport of the quantum Hall regime. Section 4 summarises the mechanisms at play in the different regimes considered. Here, we also discuss the emergence and suppression of the various peaks with antidot size and demonstrate the transition between classical and quantum regimes. Finally, a brief conclusion emphasising our key findings is given in Section 5.

2. Methods

We consider a six probe Hall bar structure as shown schematically in Fig. 1a. The main device region is constructed from a $\sim 100\text{nm}$ wide zigzag nanoribbon with a 960-atom unit cell. The six external leads consist of semi-infinite nanoribbons. A few atomic rows from the top and bottom armchair nanoribbon probes are included in the device region for mapping purposes. The main device region consists of a 4×8 array of antidots with a center-to-center separation of $D \approx 26\text{nm}$. We focus on antidots with diameter $d \approx 10\text{nm}$, as shown in this schematic, but other sizes are discussed later. The total

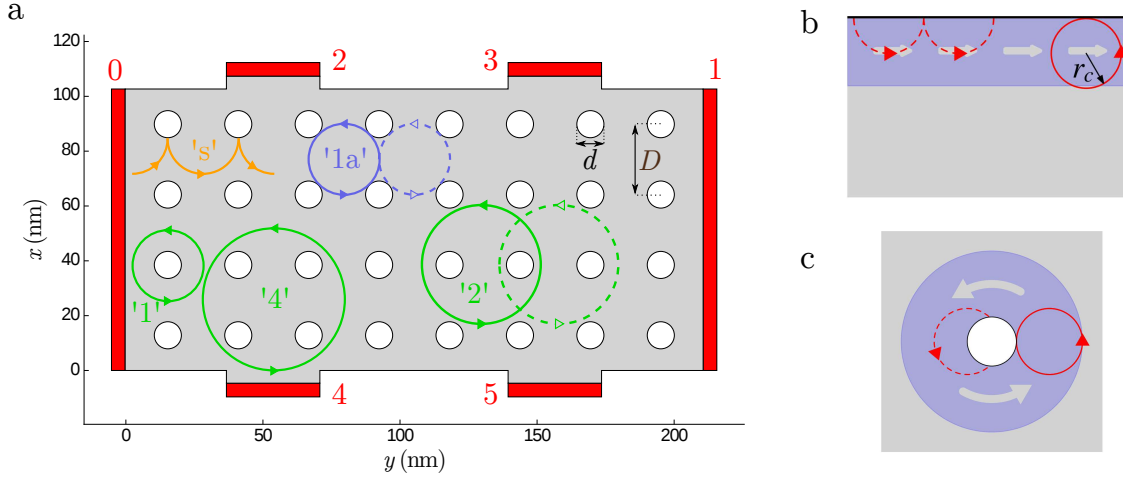


Figure 1. a) Schematic of the device geometry used for the majority of simulations in this work. The central graphene device region (grey) contains a 8×4 array of antidots with diameter $d \approx 10\text{nm}$ and separation $D \approx 26\text{nm}$. Six external leads (0–5), consisting of semi-infinite graphene nanoribbons, are shown in red. Different classical commensurability orbits are highlighted – skipping between neighbouring dots ('s', orange), pinned around dots ('1', '2', '4', green) or pinned between dots ('1a', blue). b) Dispersive edge states in the quantum Hall regime occupy the blue shaded region near an edge. Classically, these are considered as consecutive skipping orbits (dashed red trajectories) which combine to give a net current flow shown by the grey arrows. The width of the edge state region, $2r_c$, is given by the furthest extent of the cyclotron orbit which intersects the edge tangentially. c) Similarly, a *ring* of bound states forms around an antidot in a magnetic field, consisting of orbits trapped by the antidot. Unlike edge states, these are non-dispersive unless coupled to other states by additional scattering.

number of atoms in a typical simulation is between 750,000 and 950,000.

The electronic structure of the graphene is described by a single π -orbital tight-binding Hamiltonian

$$H = \sum_{\langle ij \rangle} t_{ij}(B) \hat{c}_i^\dagger \hat{c}_j, \quad (1)$$

where the sum is taken over nearest-neighbour sites only. The nearest-neighbour hopping parameter $t_{ij}(B)$ takes the value $t_{ij}(0) = t \equiv -2.7\text{eV}$ in the absence of a magnetic field. Throughout this work we will use $|t|$ as the unit of energy. The effect of a magnetic field is included using the Peierls' phase approach, which places a field-dependent phase factor into the hopping parameters

$$t_{ij}(\mathbf{B}) = t_{ij}(0) e^{\frac{2\pi i e}{h} \Theta_{ij}}, \quad (2)$$

where

$$\Theta_{ij} = \int_{\mathbf{r}_i}^{\mathbf{r}_j} \mathbf{A}(\mathbf{r}') \cdot d\mathbf{r}' \quad (3)$$

and \mathbf{r}_i is the position vector of site i and we have a choice of gauge fields \mathbf{A} which give $\mathbf{B} = \nabla \times \mathbf{A} = B\hat{z}$. The commonly used Landau gauge $\mathbf{A}_0 = -By\hat{x}$ maintains periodicity

along one direction. However, a more complicated prescription, taking advantage of periodicity in the graphene leads in both x and y directions [54], is employed for our Hall bar calculations and is outlined in more detail in Appendix A. Removing Carbon atoms from the antidot regions corresponds to the removal of the associated rows and columns from the system Hamiltonian. We also remove dangling atoms with only a single remaining neighbouring atom. Any dangling σ bonds for a Carbon atom with only two neighbouring Carbon atoms are assumed to be passivated by Hydrogen so that the π bands are unaffected.

The zero-temperature currents I_p and potentials V_p in each lead p are related via the multi-terminal Landauer-Buttiker relation

$$I_p = \frac{2e}{h} \sum (T_{qp}V_p - T_{pq}V_q), \quad (4)$$

where the transmissions are given by the Caroli formula [55]

$$T_{pq} = \text{Tr} [G^R \Gamma_q G^A \Gamma_p]. \quad (5)$$

Here, G^R and G^A are the retarded and advanced Green's functions, respectively, and Γ_p is the broadening matrix associated with lead p . Defining $\tilde{T}_{pq} = \delta_{pq} \sum_r T_{rp} - T_{pq}$ gives a direct relation $\mathbf{I} = \tilde{\mathbf{T}}\mathbf{V}$, where \mathbf{I} and \mathbf{V} are column-vectors. To calculate the longitudinal and Hall resistances, we fix a potential difference between the left and right leads, and set the net current in the top and bottom floating probes to zero. Solving for the net current flowing through the system, I , and the potentials at the top and bottom probes V_{2-5} yields the longitudinal and Hall resistances

$$R_{xx} = \frac{V_2 - V_3}{I}, \quad R_{xy} = \frac{V_2 - V_4}{I}. \quad (6)$$

The Green's functions required are calculated using efficient recursive techniques to return the matrix elements required [56, 57]. To produce spatial maps of the current density at particular values of magnetic field and Fermi energies we calculate the bond currents [56, 58, 59] between neighbouring sites i and j under the Hall bar constraints above and find

$$I_{ij}^{(n-eq.)} \sim - \sum_{p \neq 1} (V_p - V_1) \text{Im} (t_{ij}(B)(G^R \Gamma^p G^A)_{ji}). \quad (7)$$

Further details are given in Appendix B. Current heat maps in this work show the spatial distribution of current in the system, and represent the magnitude of the local current using brighter (darker) colours for larger (smaller) magnitudes. Arrows are superimposed in some zoomed current maps to illustrate the current flow direction. In both cases a spatial averaging is applied to produce current map plots with suitable resolution and clarity.

3. Commensurability peaks

Figure 2a shows the simulated longitudinal resistance R_{xx} of the $d \approx 10\text{nm}$ system shown schematically in Fig. 1a as a perpendicular magnetic field is applied. The

Fermi wavelength is fixed by gating to be much smaller than GAL length scales ($\lambda_F = \frac{\hbar v_F}{E_F} \sim 3\text{nm}$ for $E_F = 0.4|t|$) to ensure we are outside the quantum regime, i.e. $\lambda_F \simeq D, d$. The cyclotron radius, determined by the magnetic field strength, is given by

$$r_c = \frac{E_F}{v_F e B}. \quad (8)$$

The fully atomistic nature of our calculations limits the size and separation of our antidots, hence quite a large E_F is used to achieve an appropriate Fermi wavelength. This in turn requires a large magnetic field in Eq. 8 to enter the commensurability regime $r_c \sim D$. In fact, the condition $r_c = \frac{D}{2}$, associated with the primary commensurability peak occurs at $B_0 \approx 97\text{T}$ for our system. In experimental systems, $D \gtrsim 100\text{nm}$ and $d \sim 30\text{nm}$, so that the quantum to classical transition can be reached at lower Fermi energies and commensurability features accessed with $B < 10\text{T}$. The experimental and theoretical systems are directly related by scaling – from Eq. (8) we expect $B_0 \sim \frac{1}{D^2}$ when the ratio $\frac{\lambda_F}{D}$ is kept fixed – and we expect the same qualitative processes to determine electron behaviour in both. Indeed, the experimental peak observed in Ref. [52] at $B_0 \approx 3.6\text{T}$ and $\lambda_F \approx 21\text{nm}$ corresponds to $r_c \approx 54\text{nm}$ – very near the expected value $r_c = 50\text{nm}$. We plot magnetic fields in terms of B_0 for easy comparison of results at different scales and energies. In our simulations B_0 is calculated using Eq. 8. Fine oscillations, similar to those noted in Ref. [52], are superimposed on the antidot resistances. A Fourier analysis confirms these to be mostly Aharonov-Bohm in origin, with a high weight at periods $\Delta B \sim \frac{\hbar}{eA}$, where A is the area of the periodic antidot unit cell. To emphasise the commensurability peaks, a small amount of geometric disorder (random fluctuations of $\lesssim 1\text{nm}$ in the positions and radii of individual antidots) is introduced and an average taken over five such instances.

The R_{xx} curve in Fig. 2 contains (at least) three prominent peak features, which we denote as commensurability peaks C_1 , C_2 and C_3 . C_1 occurs almost precisely at B_0 . The validity of our calculations is confirmed by a direct comparison with the experimental results of Sandner *et al.* [52] in a system with $D \sim 100\text{nm}$, $d \sim 30\text{nm}$, which we reproduce with kind permission in Fig. 2b. The experimental B_0 position is set by the peak maximum. An excellent agreement is noted between simulation and experiment, suggesting a universal behaviour at different scales once the ratios between cyclotron radii and system dimensions are similar. The three peaks in R_{xx} coincide with new step-like features in R_{xy} (see Appendix C), a feature that is also visible in the experiment and in previous experimental and theoretical studies in 2DEGs [9, 10].

In an unpatterned sample, R_{xx} displays quantum Hall behaviour and is nonzero only for two scenarios: i) at discrete magnetic field values corresponding to bulk Landau levels (LL), and ii) at small magnetic field values when the edge states are not tightly-enough confined to the edges. In both cases, a breakdown of edge-only ballistic transport occurs due to the presence of states in the bulk allowing transmission between the different edges and probes. A similar mechanism lies behind the enhancement of R_{xx} in antidot devices. In the absence of edges or other scatterers, electrons in a magnetic field are

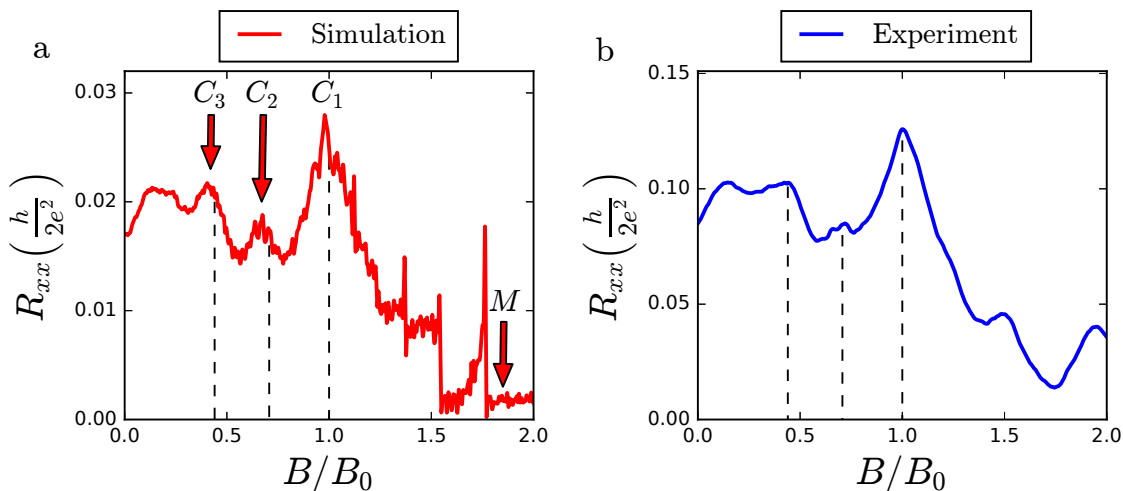


Figure 2. a) R_{xx} from a Hall bar simulation for the system in Fig. 1a at $\lambda_F \approx 3$ nm $< D, d$. The three commensurability peaks ($C_{1,2,3}$) and modified quantum Hall regime (M) are shown by the red arrows. b) The experimental R_{xx} result reproduced from Sandner *et al.* [52] – an excellent match is noted with our simulation.

localised. This is viewed semi-classically in terms of closed orbits with a given cyclotron radius r_c , whereas quantum-mechanically electrons occupy discrete LLs whose spatial extent is determined by the magnetic length l_B . In the presence of an edge, the confining potential gives dispersion to nearby states so that conducting edge states are formed for each LL. These states allow propagation in a single direction along a given edge with the total transmission at a certain Fermi energy given by the number of occupied LLs. Semi-classically, all orbits whose centers lie within r_c of the edge should scatter from it and form ‘skipping orbits’ as shown by the dashed red trajectory in Fig. 1b. In fact, the total width of the conducting edge region is excellently approximated by $2r_c$ – the furthest possible reach of an orbit which intersects the edge. This edge state region is shaded blue in Fig. 1b, with the net current flow shown by the grey arrows. Dispersive edge state formation can thus be associated with hybridisation or coupling between multiple neighbouring localised states due to scattering.

In a similar manner, the edge of an antidot also couples neighbouring localised states to create a *ring* with radius $2r_c$ beyond the edge of the antidot (i.e. total radius $2r_c + \frac{d}{2}$ from the antidot center). This region (shaded blue in Fig. 1c) can be thought of as enclosing all the semi-classical orbits which intersect an antidot. The net circulation direction is the same as that of single localised orbits and is shown in Fig. 1c by grey arrows. We note that these regions are not the same as the ‘1’-type pinned orbit (Fig. 1) which consist of single semi-classical orbits with radius r_c encircling, but not scattering from, an antidot. Unlike QHR edge states, antidot ring states are non-dispersive and bound to individual antidots in the absence of additional scattering centres. We now consider the current flow in antidot Hall bar devices as the cyclotron radius increases (magnetic field *decreases*).

3.1. Large B fields and modulated edge states

At very large magnetic fields, there is no interaction between dispersive edge states and the antidot region and the current flow is the same as without antidots. Changes in bulk state distribution, due to local antidot states breaking LL degeneracy, can manifest as a broadening of Shubnikov-de Haas oscillations in R_{xx} . Significant changes from the QHR occur when the cyclotron radius is increased so that the ring associated with an antidot intersects either another antidot or the device edge.

The separation between the top row of antidots and the system edge in our geometry is smaller than that between neighbouring antidots. As the magnetic field is decreased from the QHR, the cyclotron radius first becomes large enough to allow hybridisation between ribbon edge states and the rings associated with the first row of antidots. This modified quantum Hall regime (MQHR) is considered on the left of Fig. 3, where $B \approx 1.85B_0$. We note from Fig. 3a that the rings associated with the top row of antidots intersect the top edge, and similarly the edge state region intersects these antidots. However, while the rings of neighbouring antidots overlap, they do not intersect the neighbouring antidots themselves. Examining the current map in Fig. 3b and the zoomed region in Fig. 3c, we note that the incoming edge current from the left is split at the first antidot it encounters. The current then flows in a broader region encompassing the first row of antidots. The area enclosed by the current is a superposition of the top edge state region and the rings associated with top row antidots. New dispersive states, which now also flow around the first row of antidots, are formed by coupling between states in these regions due to edge and antidot scattering. The key factor is that the overlap region between the edge state and an antidot ring contains scatterers, namely the edge and antidot themselves. We also note that the overlap between neighbouring rings on the top row is intersected by the top edge, so that states previously bound to individual antidots can couple directly to each other due to the edge. No such hybridisation occurs between the bound states associated with nearest neighbour antidots separated vertically, as their overlap region is devoid of scatterers. The ring states of antidots in other rows thus remain localised and do not contribute to current flow in the system at this energy.

3.2. Near the principal commensurability peak

For larger r_c , the antidot rings impinge not only on the rings of neighbouring antidots, but on these antidots themselves. Semiclassically, this begins once a single orbit can cross the neck between two neighbouring antidots. This occurs from $2r_c = D - d$, corresponding to $B \approx 1.6B_0$ for the aspect ratio in this system. C_1 is prominent in our simulations between $0.8B_0 < B < 1.2B_0$ with a particularly sharp peak at $0.96B_0 < B < 1.01B_0$, suggesting that the migration of electrons between neighbouring rings contributes significantly for $B \lesssim 1.2B_0$. The extent of an antidot ring region at $B = B_0$ is shown by the dark blue shaded region around the antidot marked \mathcal{X} in Fig. 3d. The grey arrows show the net current direction in this ring. The lighter shaded

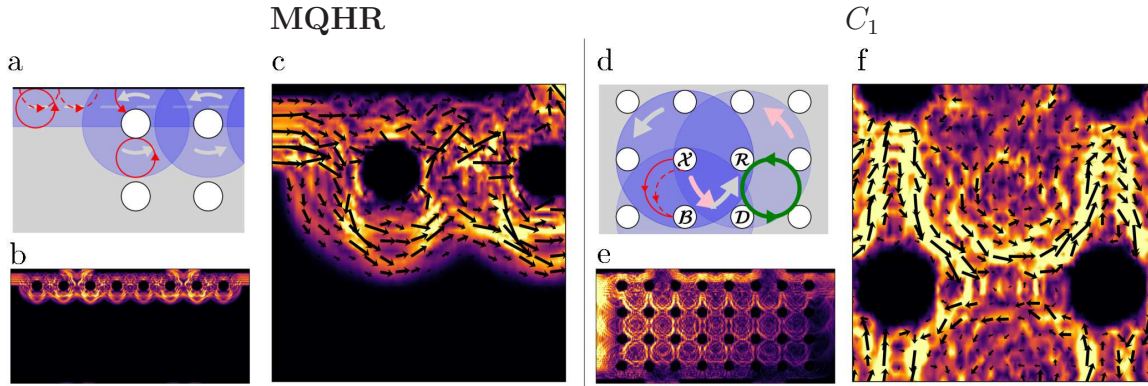


Figure 3. Schematics and current maps for the modified quantum Hall (MOHR) and first commensurability peak (C_1) regimes. a, d) Schematics showing extent of edge and/or ring states (blue shaded areas) in the given regime, net current flow directions (grey, pink arrows), and individual semi-classical trajectories (red dashed and solid lines). The thicker green circle in d) shows the expected size of the ‘1a’ type pinned orbit at this magnetic field value. b, e) Current heat maps of the entire device. c, f) Zoomed region of heat maps in (b,e) with current flow directions illustrated by arrows

region shows the ring of the antidot below (\mathcal{B}) and to the right (\mathcal{R}) of \mathcal{X} , and pale pink arrows show the current direction around \mathcal{R} . The commensurability condition $2r_c = D$, associated with simple skipping orbits (solid red curve), is also the condition for an antidot ring to entirely enclose its nearest neighbour antidots.

Let us examine the coupling between states associated with neighbouring antidots as r_c increases. In the range $D - d < 2r_c < D - \frac{d}{2}$ (or $1.6B_0 \gtrsim B \gtrsim 1.2B_0$), the ring around \mathcal{X} develops from tangentially touching \mathcal{B} to encompassing its entire top half. The portion of the antidot within the ring acts as a scatterer which can couple states associated with \mathcal{X} and \mathcal{B} . However, near the top half of \mathcal{B} , states within their respective rings have opposite orbital directions, e.g. states associated with \mathcal{X} are on average right-moving, whereas those of \mathcal{B} are left-moving. This makes it harder to scatter between rings, giving higher weight to scattering between states in the same ring and a weak coupling between states from neighbouring antidots. Current maps for B and r_c in this range show that most of the current is carried by states near the top edge and top row of antidots, similar to Fig. 3b, c, with only a minor contribution from other antidot rows. The sharp C_1 peak emerges for $D - \frac{d}{2} \lesssim 2r_c < D$ (or $1.2B_0 \gtrsim B \gtrsim 1.0B_0$), corresponding to the ring of \mathcal{X} intersecting the bottom half of \mathcal{B} . In this region, states in both rings are predominantly right-moving and a much stronger coupling is established. In semi-classical terms, the high-field edge of C_1 corresponds to the smallest orbits which can intersect both \mathcal{X} and the lower half of \mathcal{B} (the red dashed curve in Fig. 3d) C_1 reaches a maximum at B_0 , when the ring around \mathcal{X} first completely surrounds antidot \mathcal{B} due to two factors: i) the relative scattering area of \mathcal{B} in the ring overlap region reaches a maximum near here (there is a small correction towards the high field side that varies with aspect ratio), ii) the new scattering regions introduced near $B = B_0$ are particularly good at coupling states in neighbouring rings due to aligned flow directions. As r_c increases

further, the relative scattering area in the overlap region decreases rapidly, so that the relative measure of new hybridised states also decreases. Semi-classically, although we introduce additional orbits from \mathcal{X} to \mathcal{B} , we introduce more orbits which avoid \mathcal{B} altogether.

Examining the net current flow patterns at C_1 in Fig. 3e, f, it is tempting to interpret those between the top two rows of antidots as single ‘s’-type skipping orbits bouncing from the undersides of antidots in the top row. In the lower rows, an interpretation in terms of overlapping ‘1a’-type pinned orbitals or superimposed horizontal and vertical ‘s’ skips seems plausible. However, the “skipping”-type trajectory is more accurately interpreted as a hybridisation between the states of two neighbouring rings, such as those of \mathcal{X} and \mathcal{R} in Fig. 3d. The resultant current path follows the pink and grey arrows, and resembles a single skipping orbit trajectory. The circular flow pattern in lower rows emerges from a superposition of this feature with an analogous, inverted version emerging from the row of antidots underneath. This analysis is supported by examining smaller antidots, as discussed later, where the flow pattern for these trajectories takes on the triangular shape suggested by the pink and grey arrows. This shape emerges as the curvature of the rings is half that of individual skipping orbits. The circular appearance of trajectories in Fig. 3e, f emerges from two possible factors. Firstly, the aspect ratio here is $\frac{d}{D} = 0.385$ – very near to the critical value $\frac{d}{D} = \sqrt{2} - 1$, where a ring begins to intercept second nearest neighbour (2NN) antidots. This is evident in Fig. 3d, where the ring around \mathcal{X} approaches 2NN antidots (those with a diagonal separation, including that marked \mathcal{D}). This can alter the shape of the current path, and also deflect between left-to-right and top-to-bottom commensurability channels. Secondly, at these aspect ratios it is no longer possible to have completely pinned orbits of type ‘1a’ between antidots. As shown by the green orbit in Fig. 3d, these orbits now impinge upon their surrounding antidots and so join the associated ring of each antidot. The current flow at this aspect ratio therefore has a more circular character due to the hybridisation of ‘1a’-type orbits with the conducting channels.

3.3. Higher order commensurability peaks

The position of C_2 at $0.6B_0 < B < 0.75B_0$, with a maximum at $B \approx 0.68B_0$, suggests an extension of the C_1 mechanism to 2NN antidots. The condition $2r_c = \sqrt{2}D$ ($B \sim 0.71B_0$) determines when an antidot ring entirely surrounds its 2NN antidots (Fig. 4a). While this gives direct coupling between states at these antidots, it also allows for maximum hybridisation of states in the rings of *nearest neighbouring* antidots due to scattering from a third antidot. In Fig. 4a, there is increased coupling between right-moving states bound to \mathcal{X} and its neighbour to the right, \mathcal{R} , due to the presence of \mathcal{D} (and also \mathcal{B}). There is similarly increased coupling between down-moving states around \mathcal{X} and \mathcal{B} (due to \mathcal{D}' and \mathcal{L}). The grey and pink arrows (current flow around \mathcal{X} , \mathcal{R} and \mathcal{B}) suggest that this can lead to the formation of conducting channels in the

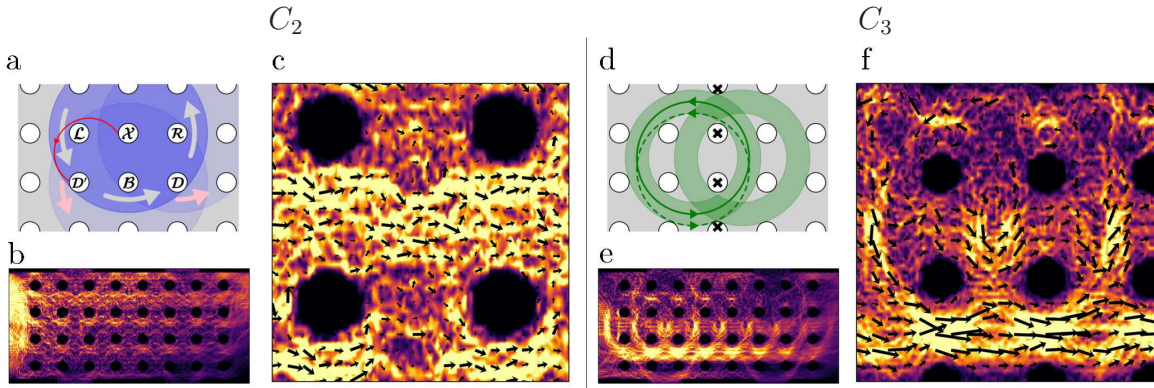


Figure 4. Same as Fig. 3, but for B and r_c corresponding to commensurability peaks C_2 (left) and C_3 (right). a, d) Schematics showing extent of ring states (blue shading) and current flow directions (grey, pink arrows), and individual classical trajectories (red and green lines). The shaded green area in d) shows the range of ‘4’ type quasi-pinned orbits which intersect one of the surrounding antidots (green dashed line). b, c, e, f) Current heat maps and zooms

rows and columns between antidots. Clear signatures of horizontal channels are seen in the current maps in Fig. 4b, c. The high-field onset of the peak at $B \sim 0.75B_0$ is smaller than the value $0.84B_0$ calculated by assuming that significant enhancement begins, as before, once orbit sizes allow scattering from the preferential side of the antidot. However, unlike the C_1 case, other antidots block many of these trajectories, particularly for smaller orbits, thus giving a narrower C_2 peak. 2NN antidots therefore influence the commensurability peaks in two ways: first by enhancing certain C_1 channels at the smallest r_c which reach them, and secondly by giving rise to C_2 channels at higher r_c .

At even larger r_c , it becomes difficult to associate rings with individual antidots. Each ring now envelopes several antidots and has large overlaps with many other rings, leading to a large degree of coupling and delocalisation. This is consistent with a wide distribution of dispersive states in the bulk, reducing the contribution of ballistic edge transport to transmission between probes 2 and 3. R_{xx} should therefore remain quite high and reasonably constant over the low field range. This prediction is confirmed in both the simulated and experimental data, further validating our analysis in terms of antidot quasi-bound states.

C_3 occurs as a reasonably wide peak between $0.3B_0 \lesssim B \lesssim 0.5B_0$, corresponding to $3.33D \gtrsim 2r_c \gtrsim 2D$. ‘4’-type pinned orbits, shown by the solid green orbit in Fig. 4d, are predicted to occur in a range centred around $B \sim 0.44B_0$ ($2r_c \sim 2.3D$). This orbit does not intersect with any antidots, so is not expected to couple with other states to become dispersive. However, a range of ‘quasi-pinned’ orbits with the same radius, but whose centers are positioned asymmetrically relative to the antidots they surround (such as that shown in dashed green) do intersect antidots. These orbits collectively fill the green shaded area surrounding the solid green orbit to form a wide four-antidot loop of hybridised states, in addition to individual localised orbits, in this region. Furthermore,

the antidots marked \mathbf{x} act to hybridise states between two neighbouring four-antidot loops. In this way, electrons can migrate through the device by circling consecutive 4-antidot loops in turn. Such behaviour is clearly visible in Fig. 4e, f, where a migrating current around groups of four antidots in the central rows of the device is noted. The net effect is to move current away from the edges and towards the centre of the device region, increasing the resistance between pairs of edge probes. At nearby fields, where clear four-ring orbits are less visible, the net effect of increasing current flow in the centre of the device, at the expense of the edge channels, is still evident.

4. Discussion

The mechanisms behind C_1 and C_2 can both be thought of as generalisations of the semi-classical ‘skipping’ orbit picture. In both cases, current percolates through a network of quasi-localised states surrounding individual antidots. For the principal commensurability peak C_1 , coupling between the states of neighbouring antidots is enhanced due to direct scattering by one antidot of electrons associated with the other. The net trajectories resemble semi-classical runaway orbits, but with a current profile that for smaller antidots has the angular shape shown in Fig. 5a. This shape is consistent with hybridisation between the rings localised around neighbouring antidots and not with a simple single skip mechanism.

In the case of C_2 , the peak is not necessarily due to a runaway orbit scenario between pairs of second nearest neighbours, but is also associated with runaway orbits between neighbouring antidots, due to scattering from 2NN antidots. We can rule out dominant contributions from ‘2’-type quasi-pinned orbits as the expected peak position for such orbits ($B \sim 0.62B_0$) is to the low-field side of the peak in our simulations.

Meanwhile, the C_3 peak emerges due to quasi-pinned type orbits, whose net effect is to divert electrons away from edge states and into channels nearer to the device center. Simulation of higher order orbits, similar to C_3 but pinned around larger groups of antidots, is non-trivial in our geometry as orbits around 9 or more antidots begin to intersect the edges of the device. Such orbits are also difficult to achieve experimentally as even greater mean-free paths are required. Nonetheless, enhancement of R_{xx} should in principle occur at these radii also. Indeed, a slight peak is present at $\sim 0.1B_0$ in both theory and experiment.

In Fig 5b, we examine the effect of varying the antidot diameter d between 5nm and 14nm, which is equivalent to aspect ratios $\frac{d}{D} \sim 0.2$ to 0.58. Each bold curve is an average over several instances of mild geometric disorder, with individual configurations shown by the lighter curves. Note that these curves are not shifted relative to each other along the R_{xx} axis, but rather the magnitude of the R_{xx} signal increases significantly with antidot size. Larger antidots act as stronger scatterers and divert more incoming edge current into the bulk of the device. C_1 at $\frac{B}{B_0} = 1$ is prominent for all but the smallest antidot diameters considered, but is particularly sharp near the $d \approx 10$ nm case considered in detail in the previous section. This may be due to the enhanced

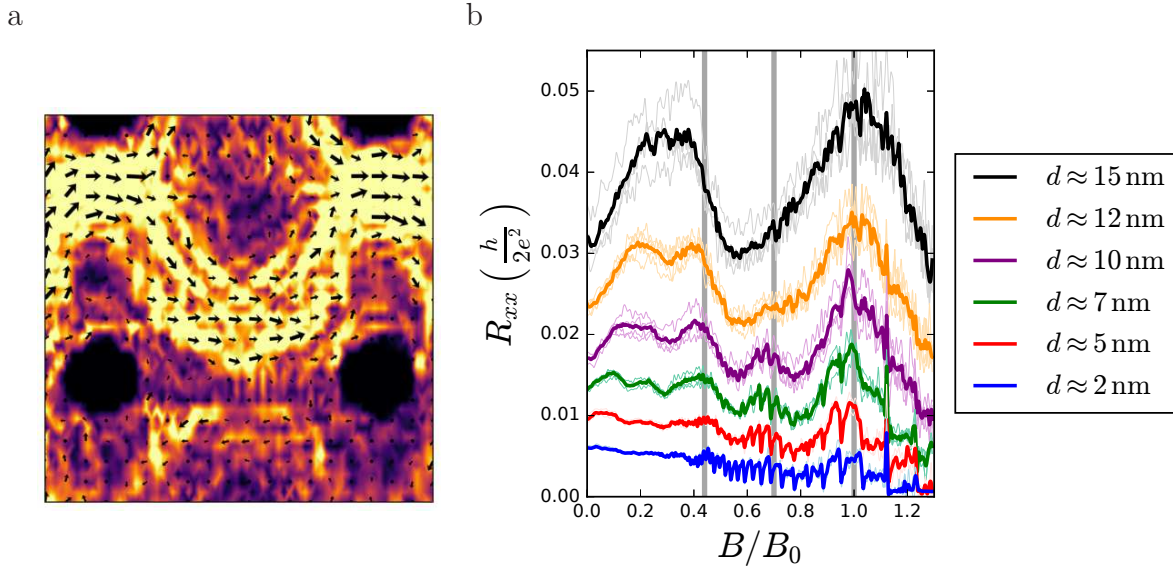


Figure 5. a) Current map zoom at C_1 for $d \approx 7\text{nm}$ showing a current path with a more angular profile than that in Fig. 3f, corresponding to flow between rings of neighbouring antidots. b) R_{xx} for a range of antidot diameters, each dark curve in an average over individual instances of mild geometric disorder (light curves). Vertical lines show the expected peak positions.

scattering caused by 2NN antidots at this aspect ratio. We note that this antidot size also gives the clearest C_2 peak. At smaller sizes, the peak is somewhat difficult to detect due to the superposition of quantum oscillations, which are related to the underlying Shubnikov-de Haas oscillations [19]. At larger sizes, it is less prominent due to the blocking effect of nearest neighbour antidots and is largely swallowed by the broadening C_1 peak. The positions of all three commensurability peaks remains quite consistent with the predicted values (grey vertical lines) over a wide range of antidot diameters.

Varying the Fermi wavelength of graphene by gating allows both the classical ($\lambda_F \ll l$, where l is a typical length scale of the system) and the quantum ($\lambda_F \sim l$) regimes to be accessed with the same sample. In Fig. 6a-d, we examine the R_{xx} response for the $d \approx 10\text{nm}$ antidot system, with and without geometric disorder, as the Fermi wavelength is increased towards the quantum regime. The red curve in these plots shows the case with no geometric disorder – the averaged and individual disordered cases are shown by the solid black and light grey curves respectively. Figure 6a, the principal case considered throughout this work, shows very little deviation between the curves, suggesting that the peak features are extremely robust against disorder. As λ_F is increased it becomes similar to d ($\sim 0.4D$) and the antidot neck width ($\sim 0.6D$) and so quantum interference effects play a more prominent role. This is reflected in the increase of sample-to-sample fluctuations in the disordered cases and a growing discrepancy between the pristine and disordered results. Figure 6e shows a plot of local current flow at $B = B_0$ for the largest λ_F considered here. The ‘skipping orbit’ current flows seen for smaller λ_F are entirely absent, and are replaced by a complex pattern of

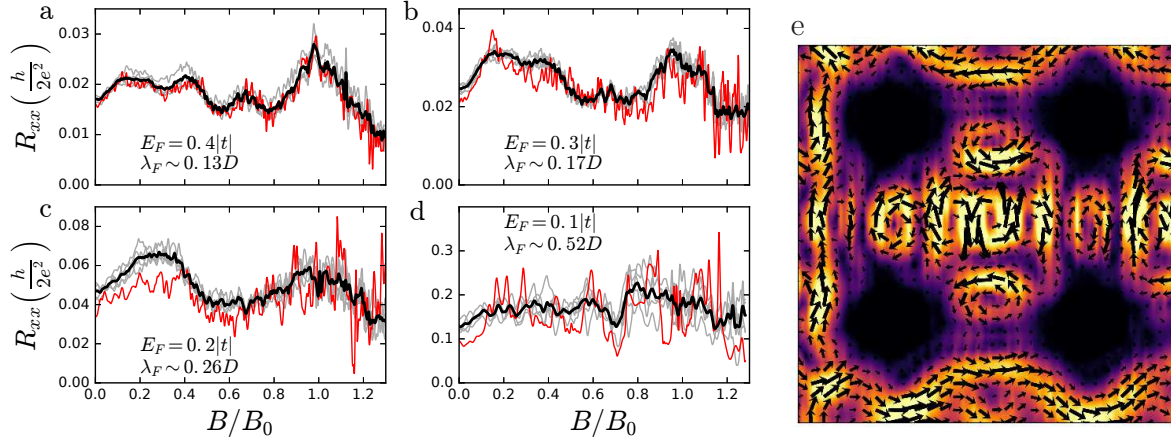


Figure 6. a-d) R_{xx} at 4 different Fermi energies, corresponding to an increase in Fermi wavelength. Red curves show the pristine system, whereas black curves are the result of averaging 5 configurations with mild position and radial disorder, with individual configurations in grey. e) Current map at $B = B_0$ for $E_F = 0.1|t|$. Skipping orbits are notably absent, replaced by vortices induced by quantum interference.

vortices arising from quantum interference effects.

5. Conclusion

We have demonstrated the emergence of magnetic commensurability effects in graphene antidot lattices from purely quantum-mechanical multi-probe transport simulations. To our knowledge, this is the first time that such a simulation has been performed for this type of system using a fully atomistic approach. Peak positions and relative magnitudes are in excellent agreement with recent ground-breaking experimental results on the same system. By examining the dependence of peak positions on cyclotron radius and aspect ratio, and by mapping the local current behaviour at important values, we are able to explain some subtle details of the mechanisms behind commensurability peaks in the longitudinal resistance. The two highest field commensurability peaks can be understood in terms of scattering between the localised states formed around individual antidots in the presence of a magnetic field. This mechanism is enhanced when these states intersect with nearest, or next-nearest, neighbouring antidots. Higher order peaks are associated with migration between quasi-pinned orbits around groups of multiple antidots, with scattering from nearby antidots again playing a key role. We also examined the evolution of the magnetoresistance as different length scales in the system are varied. The appearance of the second commensurability peak is sensitive to the antidot lattice aspect ratio. Finally, we demonstrated how the transition between classical and quantum regimes can be tuned by gating. The onset of the quantum regime at Fermi wavelengths approaching system length scales was associated with the suppression of commensurability features and a marked increase in the effect of geometric disorders. We believe that our results can act as a guide to interpreting

commensurability features in future experiments and, in particular, the role of antidot quasibound states in antidot systems.

Acknowledgments

We thank A. Sandner and J. Eroms for supplying the experimental data. The authors gratefully acknowledge the financial support from the Center for Nanostructured Graphene (Project No. DNR103) sponsored by the Danish National Research Foundation and from the QUSCOPE project sponsored by the Villum Foundation. S.R.P. acknowledges funding from the European Unions Horizon 2020 research and innovation programme under the Marie Skłodowska-Curie grant agreement No 665919 and the Severo Ochoa Program (MINECO, Grant No. SEV-2013-0295).

References

- [1] M. Katsnelson, K. Novoselov, and A. Geim. Chiral tunnelling and the Klein paradox in graphene. *Nature Physics*, 2(9):620–625, 2006.
- [2] A. F. Young and P. Kim. Quantum interference and Klein tunnelling in graphene heterojunctions. *Nature Physics*, 5(3):222–226, 2009.
- [3] K. I. Bolotin, F. Ghahari, M. D. Shulman, H. L. Stormer, and P. Kim. Observation of the fractional quantum Hall effect in graphene. *Nature*, 462(7270):196–199, 2009.
- [4] V. V. Cheianov, V. Fal’ko, and B. Altshuler. The focusing of electron flow and a Veselago lens in graphene pn junctions. *Science*, 315(5816):1252–1255, 2007.
- [5] S. Chen, Z. Han, M. M. Elahi, K. M. Habib, L. Wang, B. Wen, Y. Gao, T. Taniguchi, K. Watanabe, J. Hone, et al. Electron optics with pn junctions in ballistic graphene. *Science*, 353(6307):1522–1525, 2016.
- [6] K. S. Novoselov, A. K. Geim, S. V. Morozov, D. Jiang, Y. Zhang, S. V. Dubonos, I. V. Grigorieva, and A. A. Firsov. Electric field effect in atomically thin carbon films. *Science*, 306(5696):666–669, 2004.
- [7] B. Terrés, L. Chizhova, F. Libisch, J. Peiro, D. Jörger, S. Engels, A. Girschik, K. Watanabe, T. Taniguchi, S. Rotkin, et al. Size quantization of Dirac fermions in graphene constrictions. *Nature Communications*, 7, 2016.
- [8] T. Taychatanapat, K. Watanabe, T. Taniguchi, and P. Jarillo-Herrero. Electrically tunable transverse magnetic focusing in graphene. *Nature Physics*, 9(4):225–229, 2013.
- [9] D. Weiss, M. Roukes, A. Menschig, P. Grambow, K. von Klitzing, and G. Weimann. Electron pinball and commensurate orbits in a periodic array of scatterers. *Physical review letters*, 66(21):2790, 1991.
- [10] T. Ando and S. Uryu. Chaotic transport in antidot lattices. *Journal of Electronic Materials*, 29(5):557–564, 2000.
- [11] A. Lorke, J. P. Kotthaus, and K. Ploog. Magnetotransport in two-dimensional lateral superlattices. *Phys. Rev. B*, 44:3447–3450, Aug 1991.
- [12] R. Fleischmann, T. Geisel, and R. Ketzmerick. Magnetoresistance due to chaos and nonlinear resonances in lateral surface superlattices. *Phys. Rev. Lett.*, 68:1367–1370, Mar 1992.
- [13] S. Ishizaka and T. Ando. Detailed analysis of the commensurability peak in antidot arrays with various periods. *Phys. Rev. B*, 55:16331–16338, Jun 1997.
- [14] T. Ando, S. Uryu, and S. Ishizaka. Chaos and quantum transport in antidot lattices. *Japanese journal of applied physics*, 38(1S):308, 1999.
- [15] I. V. Zozulenko, F. A. Maaø, and E. H. Hauge. Quantum magnetotransport in a mesoscopic antidot lattice. *Phys. Rev. B*, 51:7058–7063, Mar 1995.

- [16] I. V. Zozoulenko, F. A. Maaø, and E. H. Hauge. Coherent magnetotransport in confined arrays of antidots. i. dispersion relations and current densities. *Phys. Rev. B*, 53:7975–7986, Mar 1996.
- [17] I. V. Zozoulenko, F. A. Maaø, and E. H. Hauge. Coherent magnetotransport in confined arrays of antidots. ii. two-terminal conductance. *Phys. Rev. B*, 53:7987–7995, Mar 1996.
- [18] I. V. Zozoulenko, F. A. Maaø, and E. H. Hauge. Coherent magnetotransport in confined arrays of antidots. iii. origin of the commensurate peaks. *Phys. Rev. B*, 56:4710–4715, Aug 1997.
- [19] S. Ishizaka and T. Ando. Quantum transport in square and triangular antidot arrays with various periods. *Phys. Rev. B*, 56:15195–15201, Dec 1997.
- [20] T. Nakanishi and T. Ando. Quantum interference effects in antidot lattices in magnetic fields. *Phys. Rev. B*, 54:8021–8027, Sep 1996.
- [21] P. Rakytá, E. Tóvári, M. Csontos, S. Csonka, A. Csordás, and J. Cserti. Emergence of bound states in ballistic magnetotransport of graphene antidots. *Phys. Rev. B*, 90:125428, Sep 2014.
- [22] M. R. Thomsen, S. R. Power, A.-P. Jauho, and T. G. Pedersen. Magnetic edge states and magnetotransport in graphene antidot barriers. *Phys. Rev. B*, 94:045438, Jul 2016.
- [23] M. Bieri, M. Treier, J. Cai, K. Ait-Mansour, P. Ruffieux, O. Gröning, P. Gröning, M. Kastler, R. Rieger, X. Feng, K. Müllen, and R. Fasel. Porous graphenes: two-dimensional polymer synthesis with atomic precision. *Chemical communications*, (45):6919–21, December 2009.
- [24] M. Kim, N. S. Safron, E. Han, M. S. Arnold, and P. Gopalan. Fabrication and characterization of large-area, semiconducting nanoperforated graphene materials. *Nano Letters*, 10(4):1125–31, April 2010.
- [25] J. Bai, X. Zhong, S. Jiang, Y. Huang, and X. Duan. Graphene nanomesh. *Nature Nanotechnology*, 5(3):190–4, March 2010.
- [26] M. Kim, N. S. Safron, E. Han, M. S. Arnold, and P. Gopalan. Electronic transport and Raman scattering in size-controlled nanoperforated graphene. *ACS Nano*, 6(11):9846–54, November 2012.
- [27] T. Shen, Y. Q. Wu, M. A. Capano, L. P. Rokhinson, L. W. Engel, and P. D. Ye. Magnetoconductance oscillations in graphene antidot arrays. *Applied Physics Letters*, 93(12):122102, 2008.
- [28] J. Eroms and D. Weiss. Weak localization and transport gap in graphene antidot lattices. *New Journal of Physics*, 11(9):095021, September 2009.
- [29] M. Begliarbekov, O. Sul, J. Santanello, N. Ai, X. Zhang, E.-H. Yang, and S. Strauf. Localized States and resultant band bending in graphene antidot superlattices. *Nano Letters*, 11(3):1254–8, March 2011.
- [30] A. J. M. Giesbers, E. C. Peters, M. Burghard, and K. Kern. Charge transport gap in graphene antidot lattices. *Phys. Rev. B*, 86(4):045445, July 2012.
- [31] F. Oberhuber, S. Blien, S. Heydrich, F. Yaghobian, T. Korn, C. Schuller, C. Strunk, D. Weiss, and J. Eroms. Weak localization and Raman study of anisotropically etched graphene antidots. *Applied Physics Letters*, 103(14):143111, 2013.
- [32] Q. Xu, M.-Y. Wu, G. F. Schneider, L. Houben, S. K. Malladi, C. Dekker, E. Yucelen, R. E. Dunin-Borkowski, and H. W. Zandbergen. Controllable atomic scale patterning of freestanding monolayer graphene at elevated temperature. *ACS Nano*, 7(2):1566–72, February 2013.
- [33] T. G. Pedersen, C. Flindt, J. Pedersen, N. A. Mortensen, A.-P. Jauho, and K. Pedersen. Graphene antidot lattices: Designed defects and spin qubits. *Phys. Rev. Lett.*, 100:136804, Apr 2008.
- [34] R. Petersen, T. G. Pedersen, and A.-P. Jauho. Clar sextet analysis of triangular, rectangular, and honeycomb graphene antidot lattices. *ACS Nano*, 5(1):523–9, January 2011.
- [35] J. G. Pedersen and T. G. Pedersen. Hofstadter butterflies and magnetically induced band-gap quenching in graphene antidot lattices. *Phys. Rev. B*, 87(23):235404, 2013.
- [36] J. G. Pedersen and T. G. Pedersen. Dirac model of an isolated graphene antidot in a magnetic field. *Phys. Rev. B*, 85(3):035413, 2012.
- [37] J. G. Pedersen and T. G. Pedersen. Tight-binding study of the magneto-optical properties of gapped graphene. *Phys. Rev. B*, 84:115424, 2011.

- [38] F. Ouyang, S. Peng, Z. Liu, and Z. Liu. Bandgap opening in graphene antidot lattices: the missing half. *ACS Nano*, 5(5):4023–30, May 2011.
- [39] X. Liu, Z. Zhang, and W. Guo. Universal rule on chirality-dependent bandgaps in graphene antidot lattices. *Small*, 9(8):1405–10, April 2013.
- [40] M. Vanević, V. Stojanović, and M. Kindermann. Character of electronic states in graphene antidot lattices: Flat bands and spatial localization. *Phys. Rev. B*, 80(4):045410, July 2009.
- [41] T. Gunst, T. Markussen, A.-P. Jauho, and M. Brandbyge. Thermoelectric properties of finite graphene antidot lattices. *Phys. Rev. B*, 84:155449, Oct 2011.
- [42] M. L. Trolle, U. S. Møller, and T. G. Pedersen. Large and stable band gaps in spin-polarized graphene antidot lattices. *Phys. Rev. B*, 88(19):195418, November 2013.
- [43] T. G. Pedersen and J. G. Pedersen. Transport in graphene antidot barriers and tunneling devices. *Journal of Applied Physics*, 112(11):113715, 2012.
- [44] S. S. Gregersen, J. G. Pedersen, S. R. Power, and A.-P. Jauho. Graphene on graphene antidot lattices: Electronic and transport properties. *Phys. Rev. B*, 91:115424, Mar 2015.
- [45] S. S. Gregersen, S. R. Power, and A.-P. Jauho. Robust band gap and half-metallicity in graphene with triangular perforations. *Phys. Rev. B*, 93:245429, Jun 2016.
- [46] S. Yuan, R. Roldán, A.-P. Jauho, and M. Katsnelson. Electronic properties of disordered graphene antidot lattices. *Phys. Rev. B*, 87(8):085430, February 2013.
- [47] S. Yuan, F. Jin, R. Roldán, A.-P. Jauho, and M. I. Katsnelson. Screening and collective modes in disordered graphene antidot lattices. *Phys. Rev. B*, 88(19):195401, November 2013.
- [48] V. Hung Nguyen, M. Chung Nguyen, H.-V. Nguyen, and P. Dollfus. Disorder effects on electronic bandgap and transport in graphene-nanomesh-based structures. *Journal of Applied Physics*, 113(1):013702, 2013.
- [49] X. Ji, J. Zhang, Y. Wang, H. Qian, and Z. Yu. Influence of edge imperfections on the transport behavior of graphene nanomeshes. *Nanoscale*, 5(6):2527–31, March 2013.
- [50] S. R. Power and A.-P. Jauho. Electronic transport in disordered graphene antidot lattice devices. *Physical Review B*, 90(11):115408, 2014.
- [51] Z. Fan, A. Uppstu, and A. Harju. Electronic and transport properties in geometrically disordered graphene antidot lattices. *Physical Review B*, 91(12):125434, 2015.
- [52] A. Sandner, T. Preis, C. Schell, P. Giudici, K. Watanabe, T. Taniguchi, D. Weiss, and J. Eroms. Ballistic transport in graphene antidot lattices. *Nano letters*, 15(12):8402–8406, 2015.
- [53] R. Yagi, R. Sakakibara, R. Ebisuoka, J. Onishi, K. Watanabe, T. Taniguchi, and Y. Iye. Ballistic transport in graphene antidot lattices. *Physical Review B*, 92(19):195406, 2015.
- [54] H. U. Baranger and A. D. Stone. Electrical linear-response theory in an arbitrary magnetic field: A new Fermi-surface formation. *Phys. Rev. B*, 40:8169–8193, Oct 1989.
- [55] C. Caroli, R. Combescot, P. Nozieres, and D. Saint-James. Direct calculation of the tunneling current. *Journal of Physics C: Solid State Physics*, 4(8):916, 1971.
- [56] C. H. Lewenkopf and E. R. Mucciolo. The recursive Greens function method for graphene. *Journal of Computational Electronics*, 12(2):203–231, May 2013.
- [57] M. Settnes, S. R. Power, J. Lin, D. H. Petersen, and A.-P. Jauho. Patched Green’s function techniques for two-dimensional systems: Electronic behavior of bubbles and perforations in graphene. *Phys. Rev. B*, 91:125408, Mar 2015.
- [58] A. Cresti, R. Farchioni, G. Grosso, and G. P. Parravicini. Keldysh-Green function formalism for current profiles in mesoscopic systems. *Phys. Rev. B*, 68:075306, Aug 2003.
- [59] B. K. Nikolić, L. P. Zârbo, and S. Souma. Imaging mesoscopic spin hall flow: Spatial distribution of local spin currents and spin densities in and out of multiterminal spin-orbit coupled semiconductor nanostructures. *Phys. Rev. B*, 73:075303, Feb 2006.

Appendix A. Peierls' phase approach and choice of gauge

The effect of a magnetic field on the behaviour of electrons described within a tight-binding model is included using the Peierls' phase approach. This involves placing a field-dependent phase factor into the tight-binding hopping parameters, so that

$$t_{ij}(\mathbf{B}) \rightarrow t_{ij}(0)e^{\frac{2\pi ie}{h}\Theta_{ij}}, \quad (\text{A.1})$$

where

$$\Theta_{ij} = \int_{\mathbf{r}_i}^{\mathbf{r}_j} \mathbf{A}(\mathbf{r}') \cdot d\mathbf{r}' \quad (\text{A.2})$$

$$= \int_0^1 (\mathbf{r}_j - \mathbf{r}_i) \cdot \mathbf{A}(\mathbf{r}_i + \lambda(\mathbf{r}_j - \mathbf{r}_i))d\lambda. \quad (\text{A.3})$$

Note that since the phase factor depends on the vector potential \mathbf{A} , where $\mathbf{B} = \nabla \times \mathbf{A}$, we have freedom with regard to which particular gauge to choose. For fields perpendicular to the two-dimensional plane ($\mathbf{B} = B\hat{z}$) we usually pick the Landau gauge

$$\mathbf{A}_0 = -By\hat{x}, \quad (\text{A.4})$$

which gives

$$\Theta_{ij} = -B \frac{y_i + y_j}{2}(x_j - x_i) \quad (\text{A.5})$$

$$\equiv -B\bar{y}\Delta x. \quad (\text{A.6})$$

This gauge proves useful for dealing with leads in the x -direction, as the phase term only depends on the difference in x coordinates and not their absolute value – thus periodic cells can be used within recursive Green's functions methods to calculate the self-energies for leads with this orientation. Similarly, for leads aligned with the y -axis, we can use the gauge

$$\mathbf{A}_\perp = Bx\hat{y}, \quad (\text{A.7})$$

for which

$$\Theta_{ij} = B\bar{x}\Delta y, \quad (\text{A.8})$$

which allows periodic cells in the y -direction and a phase which only depends on the absolute value of the x -coordinate.

For our Hall bar setup shown schematically in Fig. A1, containing leads with both x (0, 1) and y (2, 3, 4, 5) orientations, we follow the approach outlined by Baranger and Stone [54], which allows us to avail of periodicity in every lead of the system. We add a gauge transformation to the initial gauge in Eq. (A.4) so that

$$\mathbf{A} = \mathbf{A}_0 + \nabla\tilde{f}(x, y). \quad (\text{A.9})$$

It is clear that the magnetic field is gauge invariant under a transformation of this kind. Ideally we need a $\tilde{f}(x, y)$ which gives $\mathbf{A} = \mathbf{A}_0$ in leads 0, 1 and $\mathbf{A} = \mathbf{A}_\perp$ in leads 2–5. We define the function

$$f(x, y) \equiv Bxy \quad (\text{A.10})$$

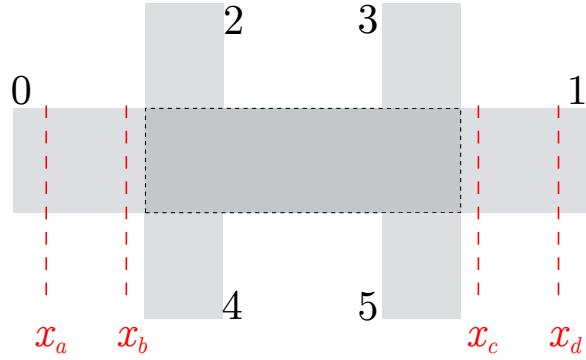


Figure A1. System schematic showing example gauge switching points.

and note that

$$\nabla f = By\hat{x} + Bx\hat{y} \quad (\text{A.11})$$

and

$$\mathbf{A} + \nabla f = \mathbf{A}_\perp, \quad (\text{A.12})$$

allowing us to switch between the two gauges of interest.

We now introduce a weight function $W(x)$ that allows us to smoothly turn on and off the gauge transformation and define

$$\tilde{f}(x, y) = W(x)f(x, y). \quad (\text{A.13})$$

W should take the value 0.0 in leads 0, 1 and value 1.0 in the other leads. Outside this regions it should vary smoothly between these values with both $W(x)$ and $W'(x) = \frac{dW}{dx}$ continuous. This gives

$$\mathbf{A} = \left\{ (W(x) - 1)By + W'(x)Bxy \right\} \hat{x} + W(x)Bx\hat{y}, \quad (\text{A.14})$$

which we can easily confirm gives the required vector potential when $W(x) = 0$ or 1 and $W'(x) = 0$, and further that $\nabla \times \mathbf{A} = B\hat{z}$ at all points.

For our Hall bar system, we include short buffer regions ($x_a < x < x_b$ and $x_c < x < x_d$ in Fig. A1) between the horizontal leads and the central device region, where we switch between the two gauges. We use a smooth step function

$$S_s(z) = 3z^2 - 2z, \quad (\text{A.15})$$

where $S_s(0) = 0$, $S_s(1) = 1$, $S'_s(0) = 0$, $S'_s(1) = 0$ to define the weight function in the different regions of our system:

$$W(x) = \begin{cases} 0 & \text{if } x \leq x_a. \\ S_s\left(\frac{x-x_a}{x_b-x_a}\right) & \text{if } x_a < x < x_b, \\ 1 & \text{if } x_b \leq x \leq x_c \\ 1 - S_s\left(\frac{x-x_c}{x_d-x_c}\right) & \text{if } x_c < x < x_d \\ 0 & \text{if } x \geq x_d \end{cases} \quad (\text{A.16})$$

With this definition, the phase factors entering in Eq. (A.1) can be written explicitly as

$$\Theta_{ij} = \begin{cases} -B \bar{y} \Delta x & \text{if } x \leq x_a. \\ \frac{B}{2L_{ab}^3} \left[\begin{aligned} &2\Delta y x_i (x_i - x_a)^2 (3L_{ab} - 2x_i + 2x_a) \\ &-\Delta x \Delta y \left(L_{ab}^3 + 4(x_i - x_a)^2 (4x_i - x_a) \right. \\ &\quad \left. - 6L_{ab} (3x_i^2 - 4x_i x_a + x_a^2) \right) \\ &-2\Delta x y_i \left(L_{ab} - x_i + x_a \right) \left(L_{ab}^2 + L_{ab} (x_i - x_a) \right. \\ &\quad \left. - 2(4x_i^2 - 5x_i x_a + x_a^2) \right) \\ &-4(\Delta x)^4 (y_i + \Delta y) \\ &+2(\Delta x)^3 (3L_{ab} - 8x_i + 6x_a) (y_i + \Delta y) \\ &+6(\Delta x)^2 \left(3L_{ab} x_i - 4x_i^2 - 2L_{ab} x_a \right. \\ &\quad \left. + 6x_i x_a - 2x_a^2 \right) (y_i + \Delta y) \end{aligned} \right] & \text{if } x_a < x < x_b, \\ B \bar{x} \Delta y & \text{if } x_b \leq x \leq x_c \\ \frac{B}{2L_{cd}^3} \left[\begin{aligned} &2\Delta y x_i (L_{cd} - x_i + x_c)^2 (L_{cd} + 2x_i - 2x_c) \\ &+\Delta x \Delta y \left(L_{cd}^3 + 4(x_i - x_c)^2 (4x_i - x_c) \right. \\ &\quad \left. - 6L_{cd} (3x_i^2 - 4x_i x_c + x_c^2) \right) \\ &+2\Delta x y_i (x_i - x_c) \\ &\quad \left(-9L_{cd} x_i + 8x_i^2 + 3L_{cd} x_c - 10x_i x_c + 2x_c^2 \right) \\ &+4(\Delta x)^4 (y_i + \Delta y) \\ &-2(\Delta x)^3 (3L_{cd} - 8x_i + 6x_c) (y_i + \Delta y) \\ &-6(\Delta x)^2 \left(3L_{cd} x_i - 4x_i^2 - 2L_{cd} x_c \right. \\ &\quad \left. + 6x_i x_c - 2x_c^2 \right) (y_i + \Delta y) \end{aligned} \right] & \text{if } x_c < x < x_d \\ -B \bar{y} \Delta x & \text{if } x \geq x_d \end{cases}$$

The validity of this choice was confirmed by reproducing the quantum Hall effect result for pristine graphene and checking the independence of local current flow on the exact positions of the gauge switching points.

Appendix B. Current maps

The current crossing a single bond between sites i and j is given in its most general form by [55, 58, 59]

$$I_{ij} = \frac{2e}{h} \int \frac{dE}{2\pi} (t_{ij} G_{ji}^< - t_{ji} G_{ij}^<), \quad (\text{B.1})$$

where the lesser Green's function can be expressed in term's of the retarded and advanced Green's functions as

$$G^<(E) = G^R(E) \Sigma^<(E) G^A(E) \quad (\text{B.2})$$

and

$$\Sigma^<(E) = i \sum_p \Gamma_p(E) f_p(E), \quad (\text{B.3})$$

where $\Gamma_p(E) = i(\Sigma_p(E) - \Sigma_p^\dagger(E))$ is the broadening and $f_p(E) = f(E - eV_p)$ is the Fermi function associated with each lead p .

With

$$G^<(E) = i \sum_p f_p(E) G^R(E) \Gamma^p(E) G^A(E) \quad (\text{B.4})$$

we can write (omitting E dependence for conciseness)

$$t_{ij} G_{ji}^< - t_{ji} G_{ij}^< = -2 \text{Im} \left[\sum_p f_p t_{ij} (G^R \Gamma^p G^A)_{ji} \right],$$

where we used $\Gamma^p = \Gamma^{p\dagger}$ and $G^A = G^{R\dagger}$.

For the two probe case, with $p = \{L, R\}$ (and assuming $\mu_L > \mu_R$)

$$\begin{aligned} \sum_p f_p G^R \Gamma^p G^A &= f_L G^R \Gamma^L G^A + f_R G^R \Gamma^R G^A \\ &= i f_R (G^R - G^A) + (f_L - f_R) G^R \Gamma^L G^A, \end{aligned}$$

which allows us to split the current into two components:

- The *persistent*, or equilibrium, current is given by

$$I_{ij}^{(pers.)} = \frac{4e}{h} \int \frac{dE}{2\pi} (f_R) \text{Re} (t_{ij} (G^R - G^A)_{ji}). \quad (\text{B.5})$$

We note that this component is independent of the chemical potential between leads, and is present even in the absence of a bias. It does not contribute to the total current through the device. Furthermore, the integration involves energies in the Fermi sea below the bias window and it is identically zero in the case of time reversal symmetry.

- The *non-equilibrium*, or total current-carrying, component is given by

$$I_{ij}^{(n-eq.)} = \frac{-4e}{h} \int \frac{dE}{2\pi} (f_L - f_R) \text{Im} (t_{ij} (G^R \Gamma^L G^A)_{ji}). \quad (\text{B.6})$$

It is carried by electrons at the Fermi surface, and vanishes in the absence of a bias. It is this current that is relevant in this work, and the bond currents plotted in this paper neglect the persistent currents which do not contribute to the overall transport measurements.

To generalise to the case of N probes, we split $G^<$ in a similar fashion to Eq. B.5 and write

$$\sum_p f_p G^R \Gamma^p G^A = i f_m (G^R - G^A) + \sum_{p \neq m} (f_p - f_m) G^R \Gamma^p G^A, \quad (\text{B.7})$$

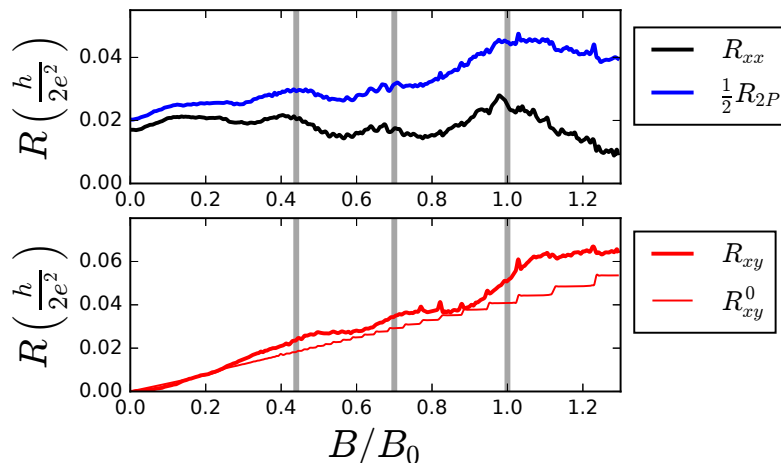


Figure C1. (Top) Comparison of R_{xx} measurement in Fig. 2a from the Hall bar setup (black) with a two-point measurement in a ribbon geometry (blue). (Bottom) Corresponding R_{xy} for the antidot system (thick red curve) and for a pristine hall bar without antidot patterning (thin red curve).

where m is chosen such that $\mu_m = \min(\mu_i)$ for $i \in \{0, \dots, N-1\}$. The total non-equilibrium bond-current in a multiterminal system is then given by

$$I_{ij}^{(n-eq.)} = \frac{-4e}{h} \int \frac{dE}{2\pi} \sum_{p \neq m} (f_p - f_m) \text{Im} (t_{ij}(G^R \Gamma^p G^A)_{ji}) . \quad (\text{B.8})$$

In this work we take the low temperature limit so that the Fermi functions become step functions. Furthermore, we assume that an infinitesimal bias is applied, so that all the quantities in Eq. B.8 are evaluated at the Fermi energy. Up to a constant, the bond currents are then given by

$$I_{ij}^{(n-eq.)} \sim - \sum_{p \neq m} (V_p - V_m) \text{Im} (t_{ij}(G^R \Gamma^p G^A)_{ji}) . \quad (\text{B.9})$$

Appendix C. Longitudinal, Hall and two-point resistance comparisons

In Fig. C1 we compare the longitudinal (R_{xx}) resistance from Fig. 2a in the main paper with a two-probe resistance measurement taken for an identical device in a nanoribbon geometry (i.e. without the top and bottom pairs of probes). We note that although signatures of the commensurability peaks are present in a two-probe measurement, they are significantly less distinct than in the Hall bar device. The Hall resistance (R_{xy}) for the antidot Hall bar device (thick red curve) shows a distinct set of step-like features emerging at the fields corresponding to commensurability peaks in R_{xx} [9, 10]. These steps are not quantised or related to the underlying quantum Hall edge states. This is clearly seen by comparing the R_{xy} for GALs with that for a pristine nanoribbon (light red curve), where the quantum Hall plateaux are clearly visible and scale very differently in height and width to the new antidot features.

The two-point measurement R_{2P} mixes the peak structure of R_{xx} with the step features of R_{xy} . Furthermore, the Hall bar setup helps to filter out contact resistance effects, which can also obscure commensurability features. Nonetheless, commensurability features, and particularly the C_1 peak, may be visible in two-probe resistances measurements of antidot lattices.